

Nacre-like surface nanolaminates enhance fatigue resistance of pure titanium

Received: 19 February 2024

Accepted: 7 August 2024

Published online: 12 August 2024

 Check for updates

Yong Zhang^{1,5}, Chenyun He^{1,5}, Qin Yu^{2,5}, Xiao Li¹, Xiaogang Wang³, Yin Zhang⁴, Ji Wang¹, Chao Jiang³, Yunfei Jia¹, Xian-Cheng Zhang¹✉, Binhan Sun¹✉, Robert O. Ritchie²✉ & Shan-Tung Tu¹

Fatigue failure is invariably the most crucial failure mode for metallic structural components. Most microstructural strategies for enhancing fatigue resistance are effective in suppressing either crack initiation or propagation, but often do not work for both synergistically. Here, we demonstrate that this challenge can be overcome by architecting a gradient structure featuring a surface layer of nacre-like nanolaminates followed by multi-variant twinned structure in pure titanium. The polarized accommodation of highly regulated grain boundaries in the nanolaminated layer to cyclic loading enhances the structural stability against lamellar thickening and microstructure softening, thereby delaying surface roughening and thus crack nucleation. The decohesion of the nanolaminated grains along horizontal high-angle grain boundaries gives rise to an extraordinarily high frequency ($\approx 1.7 \times 10^3$ times per mm) of fatigue crack deflection, effectively reducing fatigue crack propagation rate (by 2 orders of magnitude lower than the homogeneous coarse-grained counterpart). These intriguing features of the surface nanolaminates, along with the various toughening mechanisms activated in the subsurface twinned structure, result in a fatigue resistance that significantly exceeds those of the homogeneous and gradient structures with equiaxed grains. Our work on architecting the surface nanolaminates in gradient structure provides a scalable and sustainable strategy for designing more fatigue-resistant alloys.

Cyclic deformation-induced damage accumulation and the resultant catastrophic fracture of metallic materials account for nearly 90% of the failure of structural components across a broad range of safety-critical engineering sectors such as aerospace, transportation, power plants, and marine^{1–3}. Fatigue failure develops in two main stages: a) the accumulation of lattice defects (mainly dislocations) leads to strain localization which subsequently results in crack nucleation (or initiation) at local regions; b) the nucleated crack propagates driven by the

crack-tip stress field, a process that is influenced by microstructural factors (such as phase constituents, interface characteristics, stacking fault energy)^{4–8}. An ideal fatigue-resistant strategy is desired to suppress both crack initiation and propagation stages, yet the microstructural features affecting these two stages are often quite different. Accordingly, current solutions often address either crack initiation or growth, but rarely both. More specific, to suppress fatigue crack initiation, a typical approach is to strengthen materials by restricting

¹Key Laboratory of Pressure Systems and Safety, Ministry of Education, School of Mechanical and Power Engineering, East China University of Science and Technology, Shanghai 200237, China. ²Department of Materials Science and Engineering, University of California, Berkeley, CA 94720, USA. ³State Key Laboratory of Advanced Design and Manufacturing Technology for Vehicle, College of Mechanical and Vehicle Engineering, Hunan University, Changsha 410082, China. ⁴State Key Laboratory for Turbulence and Complex Systems, Department of Mechanics and Engineering Science, BIC-ESAT, College of Engineering, Peking University, 100871 Beijing, China. ⁵These authors contributed equally: Yong Zhang, Chenyun He, Qin Yu ✉ e-mail: xczhang@ecust.edu.cn; binhan.sun@ecust.edu.cn; roritchie@lbl.gov

dislocation motion through, for example, introducing dislocation-blocking interfaces⁹ and/or precipitates^{10,11}. However, such methods inevitably limit the material's capacity to blunt cracks by dislocation slip, rendering an increased crack propagation rate^{12,13}. On the other hand, the microstructure of a metallic material can be tuned to activate a variety of so-called “extrinsic” toughening mechanisms such as crack deflection, branching, microcracking, bridging, etc^{14–16}. Yet, these mechanisms operate only in the crack wake behind the crack tip, such that they can only affect crack propagation with little or no effect on crack initiation.

The recently proposed approach by designing surface-to-center gradients, in terms of a gradual change in microstructure characteristics (e.g., grain size¹⁷ or twin density¹⁸), shows some success in reconciling the above challenge^{19,20}. The fine-scaled surface structure provides high strength and limits plasticity to reduce surface roughening and suppress crack initiation²¹. The interior coarser structure, on the other hand, offers excessive dislocation accommodating ability, which is efficient for crack-tip blunting and resisting crack propagation^{17,19}. Although such gradient structures have been shown to improve fatigue resistance^{21–23}, their efficacy is often limited mainly due to the following problems: (a) the strengthened and fine-grained

(sub-)surface layers often incur abnormal grain growth under cyclic loading^{22,24}. This cyclic deformation-induced structural instability facilitates strain localization and thus promotes crack initiation^{23,25}; (b) the high-strength (sub-)surface layers have poor damage tolerance. Once the crack is nucleated, it can readily grow into a size comparable to the thickness of these (sub-)surface layers (often up to 200–800 μm)^{12,19,26}. Such short fatigue crack propagation often constitutes a considerable portion of fatigue life estimated to be up to 50% in the low-cycle fatigue regime^{27,28} and 40% in the high-cycle fatigue regime^{29,30}. Therefore, how to architect an ultrastrong (sub-) surface structure that possesses exceptional mechanical stability as well as retains good crack propagation resistance is the key to further improvements in the fatigue properties of microstructural gradient materials.

Here we introduce a gradient structure in commercial pure titanium utilizing the ultrasonic surface rolling process (USRP) technique^{31,32} (Fig. 1 and Methods). We achieved a gradient structure featuring a surface layer (<200 μm in depth) of nacre-like nanolaminated (or so-called “brick-and-mortar”) structure, which demonstrates an improved mechanical stability against grain thickening, thus offering substantial barriers for crack initiation. An ultrahigh frequency of

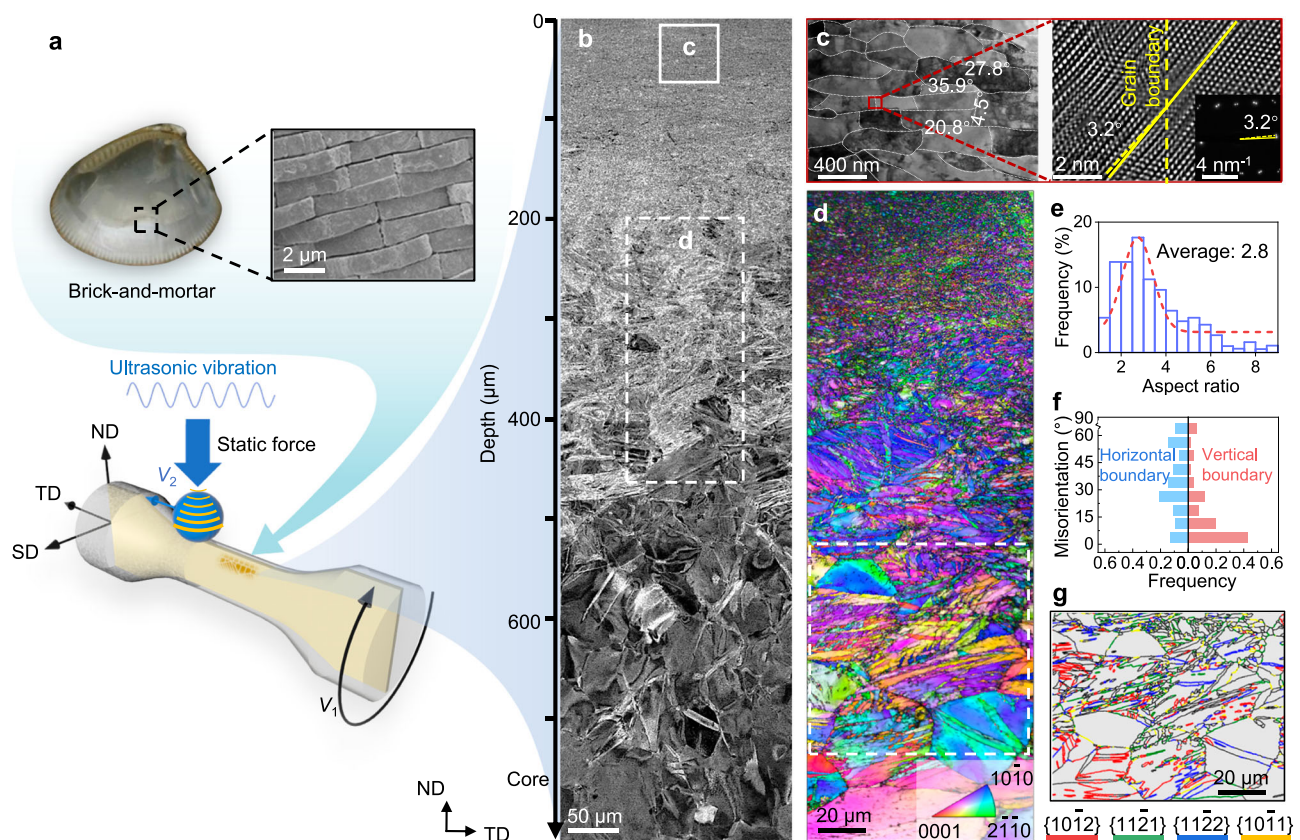


Fig. 1 | Microstructure of the surface-nanolaminated gradient Ti. **a** Schematic illustration of the ultrasonic surface rolling treatment that produces a nacre-like nanolaminated (so-called “brick-and-mortar”) structure at the topmost surface, accompanied by a *Nucula sulcata* shell and an SEM image of a typical microstructure of nacre. Reproduced with permission from refs. 57,58. Copyright⁵⁷ (2017) Springer Nature and copyright⁵⁸ (2022) Elsevier. **b** Electron channeling contrast (ECC) image showing the longitudinal view of the gradient structure spanning from the surface to a depth up to $\approx 500 \mu\text{m}$. **c** Scanning transmission electron microscopy bright-field (STEM-BF) image taken from the area roughly marked in **b**, demonstrating the nanolaminated structure at a depth of $\approx 50 \mu\text{m}$. The misorientation angle of some grain boundaries is marked. Fourier-filtered high-

resolution STEM and the corresponding Fast Fourier Transformation images taken from the marked rectangular region in **c** showing a typical vertical grain boundary with a low misorientation angle of 3.2°. **d** Electron backscatter diffraction (EBSD)-inverse pole figure (IPF) plus image quality (IQ) map of the region outlined by the dashed rectangular frame in **b**. **e** Distribution of the aspect ratio of the nanolaminates in the surface layer (at a sub-surface depth of <100 μm). **f** Distribution of the misorientation angle of the vertical and horizontal grain boundaries in the nanolaminated layer (at a sub-surface depth of $\approx 50 \mu\text{m}$). **g** EBSD interface map of the region marked by the dashed rectangular frame in **d**, showing the types of mechanical twins in the sub-surface region. Source data are provided as a Source Data file.

crack deflection of fatigue cracks subsequently enables this layer to exhibit an enhanced resistance against fatigue crack propagation that even surpasses its coarse-grained (CG) counterpart. These features, in combination with various toughening mechanisms activated in the interior gradient twinned structure, result in an improved overall fatigue resistance in comparison to the homogeneous and gradient structures with equiaxed grains.

Results and discussion

Microstructural characteristics

Figure 1b shows the longitudinal-sectional overview of the gradient structure in the pure titanium spanning from the surface to a depth of up to ≈ 500 μm . The topmost ≈ 200 - μm -thick layer features a nacre-like nanolaminated structure produced by the USRP treatment. The associated ultrahigh shear strain (up to 23.5) and shear strain rate (up to $3 \times 10^3 \text{ s}^{-1}$) imposed on the surface layer promotes the generation of dislocations and suppresses their annihilation by recovery³³. The rapid dislocation accumulation essentially induces the formation of recrystallized grains^{22,34} which are further elongated in response to the high shear deformation. The average lamellar thickness and aspect ratio are 210 nm and 2.8, respectively, remaining almost unchanged within a depth span of 10–100 μm (Fig. 1c, e). With increasing depth from ≈ 100 to 200 μm , these two values increase progressively from 210 to 500 nm and from 2.8 to 5, respectively (Supplementary Fig. 1a). Analysis of transmission electron microscopy diffraction patterns (inset in Fig. 1c) shows that the horizontal grain boundaries (oriented parallel to the lamellar direction) mostly have a high misorientation angle (above 15°) (Fig. 1f). In contrast, the vertical grain boundaries that are perpendicular to the lamellar direction have more than half of their misorientation angles below 15° (Fig. 1c, f), i.e., most of them are low-angle grain boundaries (LAGBs). The formation of these LAGBs results from the statistical mutual trapping and self-arrangement of dislocations which are promoted by the absorbed acoustic energy from the USRP treatment and the resulting enhanced dislocation motion³⁵. Such geometric arrangement of grain boundaries in these nanolaminates differs significantly from previously documented structures found in other laminated materials (e.g., pure Ni and steels^{33,36}), where mainly one grain boundary character (either high-angle or low-angle) is present^{33,36}. This unique feature contributes substantially to the mechanical stability of the surface layer which will be elaborated in the following parts. When the depth is ≈ 200 μm below the surface, the USRP-induced shear strain and strain rate are reduced to such an extent that the coarse grains cannot be sustainably refined. As a result, dense nano- and micro-sized twins are produced due to the decreased stress for twin activation in coarser grains³⁷, as shown in Fig. 1d, g (and Supplementary Fig. 1b). These twins have multiple variants, consisting mainly of {10–12} tensile and {11–22} compression twins (Fig. 1g and Supplementary Fig. 1b). The region beyond the depth of ≈ 500 μm experiences minimal USRP-induced deformation and thus maintains the original coarse grain size of 35.4 ± 8.5 μm , with only a few twins observed in the grain interior.

Fatigue resistance

Compared to a homogeneous CG structure (with an average grain size of 35.4 ± 8.5 μm), the tensile strength of the surface-nanolaminated gradient Ti is improved by ≈ 100 MPa with no sacrifice in ductility (Supplementary Fig. 2a). As shown in Fig. 2a, for the same fatigue life, the stress amplitude of surface-nanolaminated Ti is enhanced by $\approx 20\%$ compared to the CG counterpart in both low- and high-cycle regimes. This corresponds to a 10–100 times improvement in lifetime at the same stress amplitude (Fig. 2a) ranging from 243 to 202 MPa. Other than the homogeneous CG structure, we also compare the mechanical properties of the surface-nanolaminated Ti with a gradient structure having equiaxed ultrafine grains at the surface region (Supplementary Fig. 3). This latter microstructure, referred to as the gradient equiaxed-

grained (GEG) structure, was produced by reducing the surface shear strain (up to 3.8) and the surface shear strain rate (up to 10^2 s^{-1}) during the USRP treatment. Despite very similar tensile properties and near-surface residual stress of the two types of gradient structures (Supplementary Fig. 2), the surface-nanolaminated gradient Ti shows a superior fatigue resistance (improved by 5–45 times in fatigue life) compared to the GEG structure (Fig. 2a).

Fatigue crack growth (FCG) tests were further conducted to assess the crack growth resistance of the surface-nanolaminated gradient Ti. As shown in Fig. 2b, fatigue crack propagation is significantly suppressed within the nanolaminated layer, evidenced by a reduction in the FCG rate by 2–2.5 orders of magnitude compared to the homogeneous CG and GEG structures. Note that the residual compressive stress introduced by the USRP process also serves to suppress the initial growth of the fatigue crack²⁶. However, the compressive stress distribution (up to 270 MPa in the surface nanograined layer) is similar for the two gradient structures (Supplementary Fig. 2b). This indicates that the marked improvement of FCG resistance within the nanolaminated layer is solely due to its microstructural feature. It is worth mentioning that even if the residual stress is relaxed by annealing, the nanolaminated layer still exhibits enhanced resistance against fatigue crack propagation compared to its CG counterpart (Supplementary Fig. 4). These results differ fundamentally from the traditional “smaller (stronger), less-tough” trend in metallic materials, but is more akin to the toughening mechanisms exhibited in biomaterials^{38,39}, confirming the toughening potential of nacre-like nanolaminates, which will be elaborated later. After the crack propagates through the surface nanolaminated layer, the crack propagation can also be effectively retarded by the multi-variant nano- and micro-twins in the interior coarser grains, as is evident by the reduced FCG rate (by 10 times) compared to that of the CG structure (Fig. 2b).

We also plot the FCG rate at a stress intensity range of $\Delta K = 5$ MPa $\text{m}^{0.5}$, where the crack propagates inside the nanolaminated layer, as a function of its yield strength, and compare with that of other pure Ti microstructures including the homogeneous CG and ultrafine grained (UFG) structures as well as the GEG structure. The yield strength can be used as a qualitative indication on a material's fatigue strength (determined from stress-controlled testing)^{40,41} as well as its resistance to fatigue crack initiation^{12,25}. As shown in Fig. 2c, the nanolaminate in our gradient Ti possesses the highest yield strength and retains the lowest FCG rate in comparison with other counterparts, demonstrating its significant effect in improving fatigue resistance to both the crack initiation and propagation stages.

Mechanical stability

To elucidate the mechanistic role of the surface nanolaminates in the enhancement of fatigue resistance, we characterized and compared the surface microstructure before and after cyclic loading for 1.4×10^5 cycles at a stress amplitude of 216 MPa. As shown in Fig. 3a, b, the thickness of the laminated grains experiences a slight increase from 285 ± 108 nm to 366 ± 178 nm after cyclic loading (Fig. 3c). This result is in sharp contrast to that of the equiaxed ultrafine grains that typically coarsen by 3 to 10 times under cyclic loading^{22,23}. One reason for such a high stability of the nanolaminated layer (against grain thickening) is the restrained grain rotation and suppressed diffusional motion of high-angle grain boundaries (HAGBs). The rate of these two grain growth-promoting events typically decreases with a higher aspect ratio (R) of the grains, following the relationships of $d\theta dt^{-1} \propto R^{-4.42}$ and $\dot{\gamma}_B \propto R^{-1.543}$, where $d\theta dt^{-1}$ and $\dot{\gamma}_B$ represent the rate of grain rotation and the rate of boundary migration due to point defect diffusion, respectively. The absence of apparent grain rotation under cyclic loading can be further evidenced by the almost unchanged microstructural texture probed within the nanolaminated layer before and after fatigue (Fig. 3d, e).

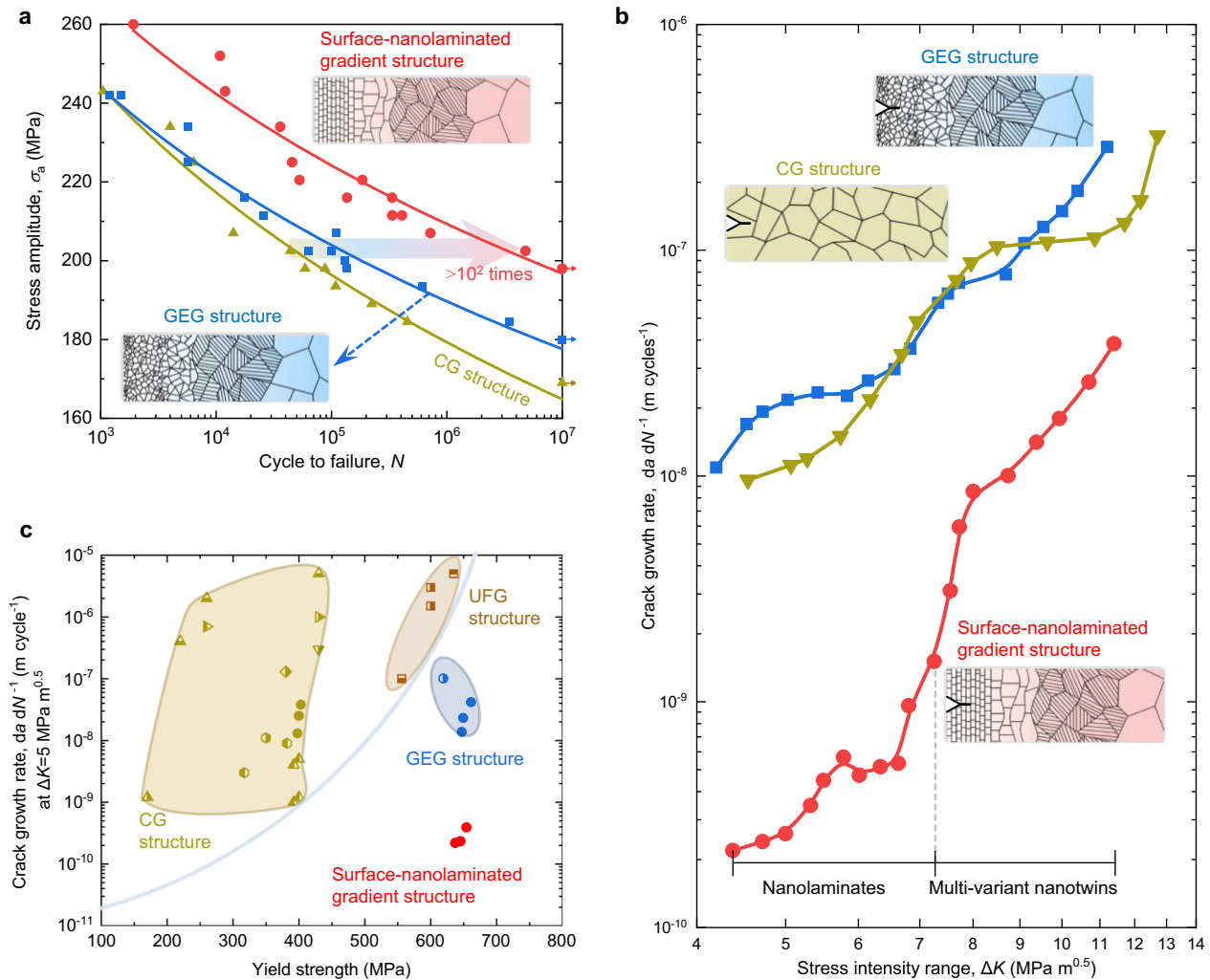


Fig. 2 | Fatigue resistance of the surface-nanolaminated gradient Ti.

a, b Number of cycles to failure plotted against stress amplitude (**a**) and fatigue crack growth rate da/dN^{-1} as a function of the applied stress intensity range ΔK for surface-nanolaminated gradient Ti, in comparison to the homogeneous coarse-grained (CG) Ti and gradient equiaxed-grained (GEG) Ti (**b**). **c** Fatigue crack growth rate at a stress intensity range of $\Delta K = 5$ MPa m $^{0.5}$ versus yield strength of pure Ti

manufactured with different microstructures. The data include homogeneous CG and ultrafine grained (UFG) structures^{12,59–63} as well as the surface nanolaminated structure (this work) and UFG structure at the surface regions of GEG Ti (this work and ref. 64.). The yield strength for the latter two microstructures was converted from the Vickers hardness value, with details shown in Supplementary Fig. 5. Source data are provided as a Source Data file.

Despite the limited thickening of the nanolaminates, it is interesting to note that their length is found to progressively increase under cyclic loading (by ≈ 2 times after 1.4×10^5 cycles at the stress amplitude of 216 MPa, Fig. 3c). This observation suggests that cyclic loading leads to movement or annihilation of vertical LAGBs. The underlying mechanism can be enlightened by revealing the fatigue-induced dynamic evolution of the vertical LAGBs with the aid of molecular dynamics (MD) simulations (full details of the simulations are given “in the Methods section” and Supplementary Fig. 6). As shown in Fig. 3h, i, under cyclic loading, partial dislocations (Supplementary Note 1) escape from the LAGBs and glide into the grain interior until they are absorbed by the horizontal HAGBs. Such a process, which is also observed in SEM/TEM experiments^{44,45}, results in a decrease in the misorientation angle between the two adjacent grains (see inset in Fig. 3g, i), which consequently induces grain merging (Fig. 3j). The ‘sacrificial’ annihilation of specific interfaces (here LAGBs), on one hand, reduces the stored energy of deformation and the system. Otherwise, the stored energy might serve as the driving force for microstructure softening, for example, by means of grain recrystallization^{22,24}. On the other hand, it essentially increases the aspect ratio of the laminated grains, which offers further restriction to

grain rotation and thus constrains the thickening of the laminated grains. This micromechanism offers another important contribution to the structural stabilization of the nanolaminates surface layer observed in this work.

Sequential toughening mechanisms

Since the lamellar thickness is the most important factor in terms of the effectiveness in blocking dislocations and hence controlling the strength of the laminated grains³³, their high mechanical stability against grain thickening renders an essential resistance to microstructural softening (Supplementary Fig. 9), a detrimental consequence that can lead to strain localization and crack initiation^{22–24}. The more intriguing feature of the stable nacre-like nanolaminate lies in its exceptional capability to resist short fatigue crack growth (Fig. 2b), which is typically lacking in high-strength materials. To reveal the underlying mechanisms, we characterized the interaction of the crack propagation path with the neighboring microstructure (Fig. 4a–e). An overview of the nature of a fatigue crack within the nanolaminated layer reveals a highly tortuous and frequently deflected propagation path (Fig. 4b). This is akin to the staircase-like cracking observed in nacre that shares a similar microstructure and is

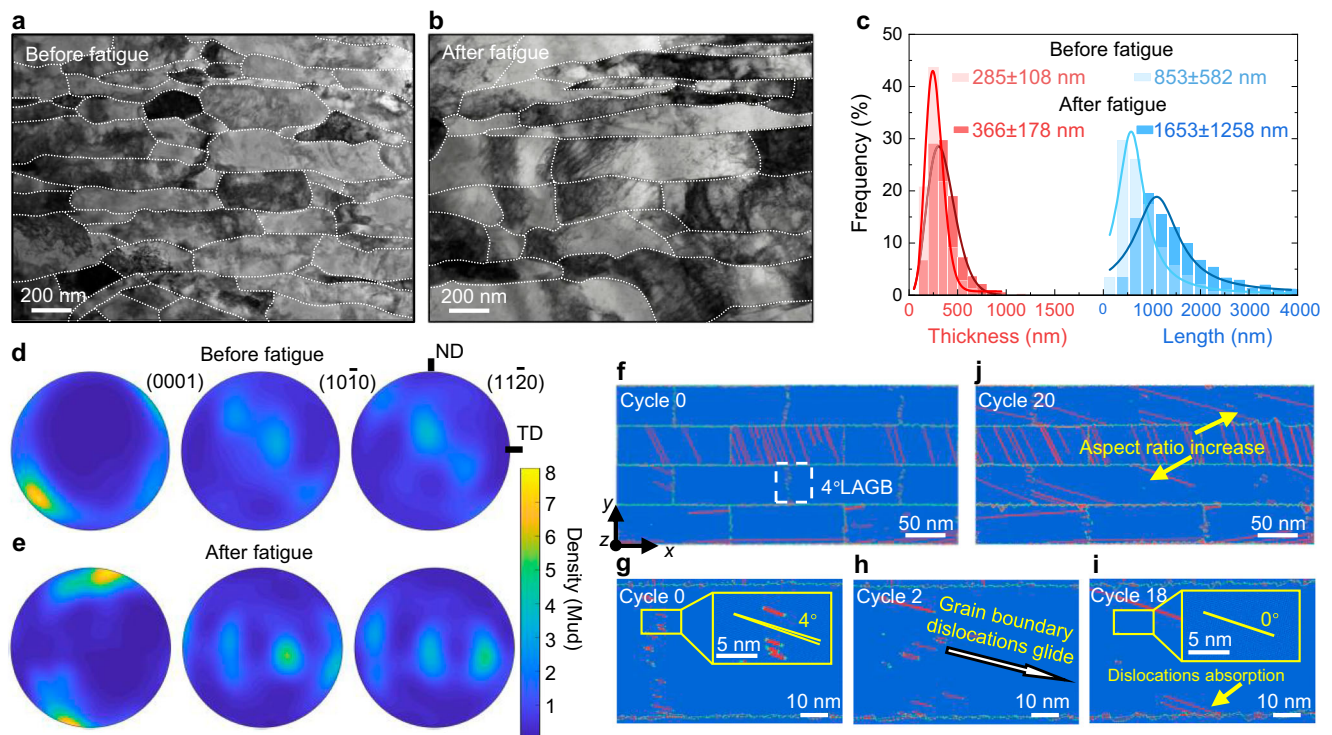


Fig. 3 | Fatigue-induced microstructural changes within the nanolaminated layer in our gradient Ti fatigue tested at the stress amplitude of 216 MPa. Representative STEM-BF images of the nanolaminates before (a) and after (b) fatigue testing (1.4×10^5 cycles). c The distribution of the thickness and length of the nanolaminates before and after fatigue, acquired from statistical analysis based on STEM images. EBSD pole figures taken from the nanolaminated region before (d) and after (e) fatigue testing, showing an almost unchanged texture. Multiple

uniform distribution (Mud), a measure of crystallographic orientation distribution, is an exactly equivalent unit. Atomic simulations revealing the configurations of the interfaces in the nanolaminates before (f) and after (j) cyclic loading, in which the hexagonal close-packed (HCP), face-centered cubic (FCC) and non-structure atoms are colored blue, red and cyan, respectively. g–i Magnified fatigue-induced dynamic evolution of the vertical LAGBs outlined by the dashed rectangular frame in f. Source data are provided as a Source Data file.

known to be fatigue resistant⁴⁶. In contrast to the transgranular cracking often observed in CG Ti³⁰, more than 80% of the crack advance in the nanolaminated region is along grain boundaries (Fig. 4c–e and Supplementary Fig. 10). The intergranular cracking originates from the high stress concentration developed at the grain boundary regions during cyclic loading. Due to the limited slip systems and twinning activity in the ultrafine grains with a HCP structure³⁷, such stress concentration is difficult to be relieved by plastic deformation, which in turn gives rise to grain boundary decohesion. The intergranular cracking of the mechanically-stable nacre-like nanolaminates ensures a high crack deflection angle (nearly 90° in most cases, as shown in Fig. 4b, c, e). The 90° crack deflection results in a highly efficient crack deflection induced toughening^{14,38} with a more pronounced roughness-induced crack closure effect⁴⁷ compared to the case in equiaxed grains. Based on linear elastic fracture mechanics analysis⁴⁸ (Supplementary Fig. 11 and Supplementary Note 2), double 90° crack deflections cause a significant reduction of the effective stress intensity factor by roughly 44%, in comparison to only a 14% reduction in the case of 60° crack deflections for the equiaxed grained structure. Furthermore, due to the nano-sized thickness of the nanolaminated layer ($\approx 210 \pm 40$ nm), the intergranular cracking along the nanolaminates boundaries results in extraordinarily high frequency of crack deflection, which is estimated to be $\approx 1.7 \times 10^3$ times per mm (Supplementary Fig. 12). This highly frequent crack deflection strongly suppresses the early-stage fatigue crack growth, which explains the markedly reduced FCG rate of the surface-nanolaminated gradient Ti compared with the GEG counterpart at ΔK below 7 MPa m^{0.5} (Fig. 2b).

In addition to the suppressed crack growth within the surface nanolaminated layer, we find that the subsequent multi-variant

twinning layer can further resist fatigue crack growth, as evidenced by the reduced FCG rate in this crack propagation stage (Fig. 2b). As the crack approaches the densely twinned region, the propagation path changes to an intragranular mode with less frequent deflection (Fig. 4e). Instead, crack arrest and blunting accompanied by numerous dislocation emission near the twin boundaries are observed (Fig. 4f–h). Sometimes, the blocking effect of the twin boundaries on the crack advance results in a bifurcated plastic zone¹⁶, thereby intensifying the extent of crack branching (Supplementary Fig. 13). These twin-associated toughening effects constitute another distinct (although not dominant) contribution (Fig. 4i) to the overall fatigue resistance in our gradient Ti (Fig. 2a).

To conclude, while demonstrated to be beneficial for fatigue resistance in certain cases^{22,24}, the traditional gradient equiaxed-grained structure suffers from mechanical instability and poor damage tolerance at the surface strengthened layer. Our work shows that this drawback can be addressed by architecting a surface layer (≈ 200 μ m) of nacre-like nanolaminates. In contrast to ultrafine equiaxed-grained structure, such surface nanolaminates exhibit a high mechanical stability against grain thickening, thus resisting plastic deformation at the surface layer that is crucial for crack initiation resistance. The rate of crack propagation within this surface layer is efficiently reduced (by up to 2 orders of magnitude), due to the highly frequent fatigue crack deflections ($\approx 1.7 \times 10^3$ times per mm) induced by interfacial decohesion. These observations thus demonstrate that both fatigue crack initiation and early-stage crack propagation can be simultaneously suppressed within one type of microstructural constituent. This feature, in combination with a variety of toughening mechanisms activated in the interior twinned coarser gradient structure, results in a marked improvement in

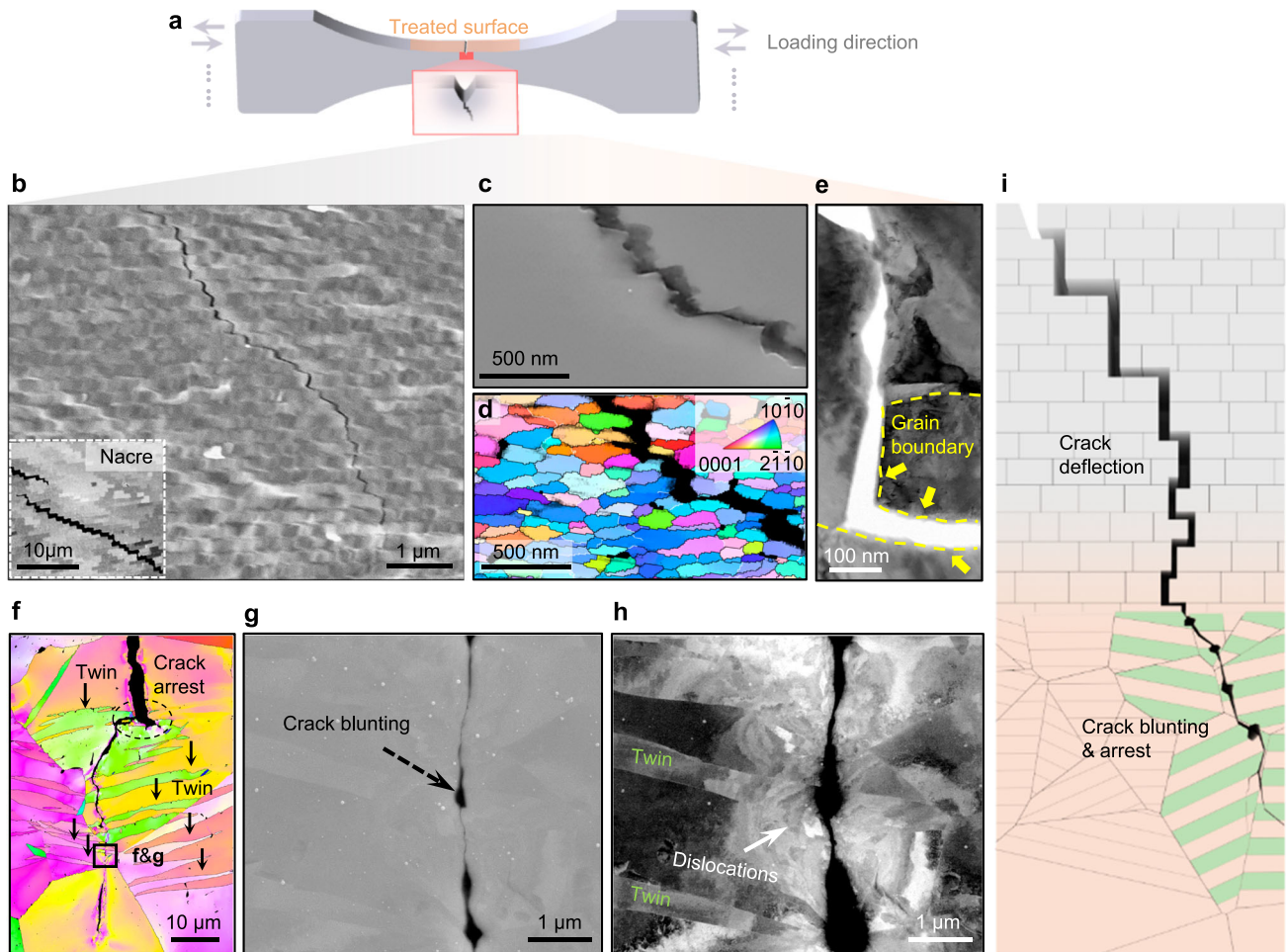


Fig. 4 | Fatigue crack path profile in the surface-nanolaminated gradient Ti.

a Schematic illustration of the USRP treated sample with a single-edge notch under fatigue loading. **b** Fatigue crack path in the nanolaminated layer, showing frequent staircase-like crack deflection similar to the cracking behavior observed in nacre as inset (reproduced with permission from ref. 65, CC BY 4.0). Secondary electron (SE) image (**c**) and the corresponding EBSD-IPF plus IQ map (**d**), and STEM-BF image of a

magnified region of the deflected crack (**e**), showing the intergranular cracking along the nanolaminates boundary. **f** EBSD-IPF map of the fatigue crack within the densely twinned layer, with IPF coloring corresponding to that in **d**. SE image (**g**) and the corresponding ECC image (**h**) taken from the region marked in **f**, showing crack blunting at the twin boundaries. **i** Schematic illustration of the crack-resisting mechanisms at different stages of fatigue cracking.

overall fatigue resistance (up to ≈ 100 times in fatigue life) in comparison to the homogeneous structures and other gradient Ti without having such surface nanolaminates. Therefore, in addition to the reported beneficial effect of nanolaminated structure on thermal stability⁴⁶ and tensile strength-ductility combination³⁶, we successfully extend this microstructural strategy to the realm of fatigue. The presented design paradigm, also anticipated to be applicable for commercial alloys (such as Ti- and Ni-based alloys), can be readily scaled up for application in enhancing and rejuvenating fatigue performance of large complex structural components like compressor blades^{31,32}, thus demonstrating a promising economic and sustainable impact in the field of fatigue resistance.

Methods

Sample preparation

The material investigated in this study is commercial pure titanium (TA2), which is composed of a single α -phase with equiaxed grains (average size of $\approx 35 \mu\text{m}$). The raw materials in the form of sheet were machined into dog-bone shaped cylindrical rods (gauge diameter 4 mm). The ultrasonic surface rolling process (USR) was applied at ambient temperature on the whole gauge section. During USRP, a static extrusion force with ultrasonic vibration was imposed to the sample surface. The detailed parameters of

the USRP process are: static force 800 N, rotational speed 750 rounds min^{-1} , vibration amplitude $10 \mu\text{m}$, axial feeding rate 10 mm min^{-1} , frequency of ultrasonic mechanical vibration 20 kHz, and processing times 4.

The ultrahigh shear strain (up to 23.5) and shear strain rate (up to $3 \times 10^3 \text{ s}^{-1}$) imposed by the USRP treatment promotes the generation of dislocations (particularly geometrically necessary dislocations (GNDs) that need to accommodate the high strain gradient of up to $\approx 5.7 \times 10^5 \text{ m}^{-1}$) and suppresses their annihilation by recovery³³. The simultaneous intervention of high-frequency ultrasonic impact (intensity of $2.1 \times 10^3 \text{ W cm}^{-2}$) introduces an oscillatory stress and acoustic softening effect, which also increases the dislocation multiplication rate and mobility while inhibiting the formation of severe deformation-induced damage⁴⁹. The high dislocation generation speed and the suppressed dynamic recovery essentially induce the formation of recrystallized grains which further become elongated as a response to the high shear deformation, generating nano-scaled laminated grains in the surface layer.

Mechanical testing

The dog-bone sheet samples for tensile and fatigue testing were machined from the USRP treated dog-bone rods (Fig. 1a). The gauge dimensions of the tensile and fatigue specimens were $10 \text{ mm} \times 4$

mm × 2 mm and 8 mm × 4 mm × 1 mm, respectively. Tensile tests were conducted using an Instron 8801 servo-hydraulic testing machine (Instron Corporation, Norwood, MA, USA) at a constant crosshead speed corresponding to a nominal strain rate of $5 \times 10^{-4} \text{ s}^{-1}$. The uniaxial tension-tension fatigue tests were carried out with a frequency of 10 Hz and a stress ratio of 0.1 at ambient temperature. The surface of both untreated and USPR treated samples for fatigue testing was carefully polished using a wool felt wheel to ensure the same surface roughness. The thickness of the removed surface due to polishing is less than 5 μm. Fatigue crack growth tests were performed on fatigue specimens with a single-edge notch (30 μm in depth) under the conventional ΔK -increasing condition based on ASTM Standard E647-15e1⁵⁰. An SEM built-in fatigue testing system (Shimadzu SEM-Servo Pulser) was employed to enable in-situ observation of the crack path during the fatigue process. To eliminate the mechanical notch effect, a moderate load (maximum stress 260 MPa) was applied to carefully produce a pre-crack with a length of $\approx 20 \mu\text{m}$ at the notch tip prior to the start of data acquisition. Fatigue tests were conducted at room temperature using a constant amplitude sinusoidal loading with an applied stress ratio of 0.1 and a loading frequency of 10 Hz. The nominal stress intensity range ΔK was calculated based on Eqs. (1) and (2)⁵¹:

$$K = \Delta\sigma\sqrt{\pi a}F\left(\frac{a}{W}\right) \quad (1)$$

$$F\left(\frac{a}{W}\right) = 0.265\left(1 - \frac{a}{W}\right)^4 + \left(0.857 + 0.265\frac{a}{W}\right)\left(1 - \frac{a}{W}\right)^{3/2} \quad (2)$$

where W is the width of the sample and is the applied stress range. The real-time crack length a was recorded based on in-situ SEM observation. The crack propagation rate was determined using the 7-point incremental polynomial method documented in ASTM Standard E647-15e1⁵⁰. Fatigue testing was terminated when the microcrack propagated to a depth of $\approx 500 \mu\text{m}$, which corresponds to the depth of the deformation layer in the gradient structure. For all mechanical testing conducted in this study, at least two samples were tested to ensure the repeatability.

Microstructure characterization

The microstructure of the specimens before and after fatigue testing and the crack trajectory were characterized using secondary electron (SE) imaging, electron channeling contrast imaging (ECCI) and electron backscatter diffraction (EBSD) (using a Zeiss-Merlin and a Zeiss Crossbeam 340 scanning electron microscopy (SEM) instrument). Samples for EBSD and ECCI were finally polished with a 0.05 μm colloidal silica suspension containing 30 vol.% H₂O₂. The acquired EBSD data (grain size, local misorientation and twin interface) were analyzed using the TSL OIM software package.

The microstructure details of the surface nanolaminates and the fatigue cracks within them were examined using a transmission electron microscope (TEM, FEI Talos F200X, operated at 200 kV). The samples for TEM before and after fatigue testing were ground and mechanically polished with SiC papers down to a thickness of 80 μm. Areas near the rolling face of the USRP treated specimen was then carefully thinned by ion milling to characterize each region of the gradient structure. Double beam ion thinning was conducted using a 1051 TEM Mill Fischione machine (Fischione Instruments, Pittsburgh, PA, USA) at 6 kV Ar⁺ ions with an incidence angle of 8°. The misorientation angle of grain boundaries within surface nanolaminates was determined based on the diffraction patterns of the adjacent two grains⁵². The crack-tip regions within the nanolaminates for TEM observation were processed at 30 kV and 2–6 nA with Ga ion sources. Final milling was performed with a 2 kV and 24 pA Ga ion beam.

Nano-indentation tests were performed on a Bruker Hysitron TriboScope, using a Berkovich shaped indenter with a load of 100 mN. Residual stress assessment was carried out using a Proto-I X-ray Diffraction (XRD) MG40P FS STD residual stress tester with Cu-K α radiation at a wavelength of 1.5406 Å. An electrochemical polishing technique using an etching solution comprised of 10 vol.% HClO₄ (70% purity) and 90 vol.% CH₃OH (99.9% purity) was adopted to remove the material layer by layer. The XRD measurement parameters were set to an acceleration voltage of 20 kV and a current of 4 mA. Data analysis was carried out using the $\sin(2\varphi)$ method⁵³, with a Bragg angle of 142° and selection of the {213} diffraction crystal plane of the α -phase.

Atomistic simulations

MD simulations were carried out using the Large-scale Atomic/Molecular Massively Parallel Simulator (LAMMPS)⁵⁴ and the embedded atom method (EAM) potentials for Ti⁵⁵. The constructed model consisted of twelve grains, with dimensions of 420 nm in length, 200 nm in height, and 4.425 nm in thickness. The total number of atoms in the simulation was $\approx 21,000,000$. Periodic boundary conditions were applied in all three directions. The initial structure was first energy minimized using a conjugate-gradient algorithm, and then relaxed at 300 K using a Nose–Hoover thermostat for 50 ps in the constant temperature constant volume (NVT) ensemble and 100 ps in the constant pressure constant temperature constant pressure (NPT) ensemble to stabilize the microstructure. During the fatigue loading, the model was under the NPT ensemble at 300 K. The stress-controlled cyclic loading was applied in the direction that was parallel to the laminated direction with a constant stress ratio of 0.1. The Ovito software⁵⁶ was used to visualize the model and analyze the data.

Data availability

The data that support the findings of this study are available from the corresponding author upon request. Source data are provided with this paper.

References

- Suresh, S. *Fatigue of materials* (Cambridge university press, 1998).
- Schijve, J. *Fatigue of structures and materials* (Springer Dordrecht, 2009).
- Campbell, F. C. *Fatigue and fracture: Understanding the basics* (ASM International, 2012).
- Krupp, U. *Fatigue crack propagation in metals and alloys: microstructural aspects and modelling concepts* (John Wiley & Sons, 2007).
- McEvily, A. Jr & Boettner, R. On fatigue crack propagation in FCC metals. *Acta Met.* **11**, 725–743 (1963).
- Yang, H. K., Doquet, V. & Zhang, Z. F. Fatigue crack growth in two TWIP steels with different stacking fault energies. *Int. J. Fatigue* **98**, 247–258 (2017).
- Suresh, S. & Ritchie, R. O. Propagation of short fatigue cracks. *Int. Met. Rev.* **29**, 445–475 (1984).
- Li, L., Zhang, Z., Zhang, P. & Zhang, Z. A review on the fatigue cracking of twin boundaries: Crystallographic orientation and stacking fault energy. *Prog. Mater. Sci.* **131**, 101011 (2023).
- Cavaliere, P. Fatigue properties and crack behavior of ultra-fine and nanocrystalline pure metals. *Int. J. Fatigue* **31**, 1476–1489 (2009).
- Zhang, Q., Zhu, Y., Gao, X., Wu, Y. & Hutchinson, C. Training high-strength aluminum alloys to withstand fatigue. *Nat. Commun.* **11**, 5198 (2020).
- Sun, B. et al. Physical metallurgy of medium-Mn advanced high-strength steels. *Int. Mater. Rev.* **68**, 786–824 (2023).
- Hanlon, T., Tabachnikova, E. & Suresh, S. Fatigue behavior of nanocrystalline metals and alloys. *Int. J. Fatigue* **27**, 1147–1158 (2005).

13. Hanlon, T., Kwon, Y.-N. & Suresh, S. Grain size effects on the fatigue response of nanocrystalline metals. *Scr. Mater.* **49**, 675–680 (2003).
14. Zhang, M. et al. On the damage tolerance of 3-D printed Mg-Ti interpenetrating-phase composites with bioinspired architectures. *Nat. Commun.* **13**, 3247 (2022).
15. Ritchie, R. O. Mechanisms of fatigue crack propagation in metals, ceramics and composites: Role of crack tip shielding. *Mater. Sci. Eng., A* **103**, 15–28 (1988).
16. Gao, Y., Stölken, J. S., Kumar, M. & Ritchie, R. O. High-cycle fatigue of nickel-base superalloy René 104 (ME3): Interaction of microstructurally small cracks with grain boundaries of known character. *Acta Mater.* **55**, 3155–3167 (2007).
17. Fang, T., Li, W., Tao, N. & Lu, K. Revealing extraordinary intrinsic tensile plasticity in gradient nano-grained copper. *Science* **331**, 1587–1590 (2011).
18. Cheng, Z., Zhou, H., Lu, Q., Gao, H. & Lu, L. Extra strengthening and work hardening in gradient nanotwinned metals. *Science* **362**, eaau1925 (2018).
19. Cao, R. et al. On the exceptional damage-tolerance of gradient metallic materials. *Mater. Today* **32**, 94–107 (2020).
20. Lei, Y. B., Wang, Z. B., Xu, J. L. & Lu, K. Simultaneous enhancement of stress- and strain-controlled fatigue properties in 316L stainless steel with gradient nanostructure. *Acta Mater.* **168**, 133–142 (2019).
21. Long, J. et al. Improved fatigue resistance of gradient nanograined Cu. *Acta Mater.* **166**, 56–66 (2019).
22. Li, X. et al. Elucidating the effect of gradient structure on strengthening mechanisms and fatigue behavior of pure titanium. *Int. J. Fatigue* **146**, 106142 (2021).
23. Yang, L., Tao, N. R., Lu, K. & Lu, L. Enhanced fatigue resistance of Cu with a gradient nanograined surface layer. *Scr. Mater.* **68**, 801–804 (2013).
24. Pan, Q. S., Long, J. Z., Jing, L. J., Tao, N. R. & Lu, L. Cyclic strain amplitude-dependent fatigue mechanism of gradient nanograined Cu. *Acta Mater.* **196**, 252–260 (2020).
25. Padilla, H. A. & Boyce, B. L. A Review of Fatigue Behavior in Nanocrystalline Metals. *Exp. Mech.* **50**, 5–23 (2009).
26. Wang, Y. et al. The influence of combined gradient structure with residual stress on crack-growth behavior in medium carbon steel. *Eng. Fract. Mech.* **209**, 369–381 (2019).
27. Wang, J. et al. Multi-stage dwell fatigue crack growth behaviors in a nickel-based superalloy at elevated temperature. *Eng. Fract. Mech.* **253**, 107859 (2021).
28. MacLachlan, D. W., Karamitros, V. & Dunne, F. P. E. Mechanistic modelling of fatigue nucleation and short crack growth in polycrystalline alloys. *J. Mech. Phys. Solids* **177**, 105314 (2023).
29. Santus, C. & Taylor, D. Physically short crack propagation in metals during high cycle fatigue. *Int. J. Fatigue* **31**, 1356–1365 (2009).
30. Tao, Z., Chang, L., Li, J., Lv, C. & Zhou, C. In-situ experimental investigation of the small fatigue crack behavior in CP-Ti: The influence of micronotch size. *Int. J. Fatigue* **175**, 107755 (2023).
31. Zhang, K. et al. Coordinated motion planning in a double-sided tools system with surface uniformity requirements. *J. Manuf. Process.* **70**, 470–483 (2021).
32. Zhang, K. et al. Coordinated bilateral ultrasonic surface rolling process on aero-engine blades. *Int. J. Adv. Manuf. Technol.* **105**, 4415–4428 (2019).
33. Liu, X. C., Zhang, H. W. & Lu, K. Strain-induced ultrahard and ultrastable nanolaminated structure in nickel. *Science* **342**, 337–340 (2013).
34. Wen, M., Liu, G., Gu, J.-F., Guan, W.-M. & Lu, J. Dislocation evolution in titanium during surface severe plastic deformation. *Appl. Surf. Sci.* **255**, 6097–6102 (2009).
35. Langenecker, B. Effects of ultrasound on deformation characteristics of metals. *IEEE Trans. Sonics Ultrason* **13**, 1–8 (1966).
36. Shang, Z. et al. Gradient nanostructured steel with superior tensile plasticity. *Sci. Adv.* **9**, eadd9780 (2023).
37. Ghaderi, A. & Barnett, M. R. Sensitivity of deformation twinning to grain size in titanium and magnesium. *Acta Mater.* **59**, 7824–7839 (2011).
38. Ritchie, R. O. The conflicts between strength and toughness. *Nat. Mater.* **10**, 817–822 (2011).
39. Koester, K. J., Ager, J. W. & Ritchie, R. O. The true toughness of human cortical bone measured with realistically short cracks. *Nat. Mater.* **7**, 672–677 (2008).
40. Kim, W.-J., Hyun, C.-Y. & Kim, H.-K. Fatigue strength of ultrafine-grained pure Ti after severe plastic deformation. *Scr. Mater.* **54**, 1745–1750 (2006).
41. Villechaise, P. et al. Effect of Stress Ratio and Notch on Fatigue Strength of Commercial Pure Titanium. *MATEC Web Conf.* **321**, 11012 (2020).
42. Harris, K., Singh, V. & King, A. Grain rotation in thin films of gold. *Acta Mater.* **46**, 2623–2633 (1998).
43. Raj, R. & Ashby, M. On grain boundary sliding and diffusional creep. *Metall. Trans.* **2**, 1113–1127 (1971).
44. Gu, H. et al. Orientation dependence of cyclic deformation in high purity titanium single crystals. *Mater. Sci. Eng., A* **188**, 23–36 (1994).
45. Chen, Y. et al. Coordinated grain boundary deformation governed nanograin annihilation in shear cycling. *J. Mater. Sci. Technol.* **86**, 180–191 (2021).
46. Gao, H. L. et al. Mass production of bulk artificial nacre with excellent mechanical properties. *Nat. Commun.* **8**, 287 (2017).
47. Suresh, S. & Ritchie, R. O. A geometric model for fatigue crack closure induced by fracture surface roughness. *Metall. Trans. A* **13**, 1627–1631 (1982).
48. Cotterell, B. & Rice, J. Slightly curved or kinked cracks. *Int. J. Fract.* **16**, 155–169 (1980).
49. Siu, K. W., Ngan, A. H. W. & Jones, I. P. New insight on acousto-plasticity – Ultrasonic irradiation enhances subgrain formation during deformation. *Int. J. Plast.* **27**, 788–800 (2011).
50. ASTM. *E647-15e1 Standard Test Method for Measurement of Fatigue Crack Growth Rates* (ASTM, 2015).
51. Tada, H., Paris, P. & Irwin, G. *The stress analysis of cracks handbook*, 3rd ed. (ASME Press, 2000).
52. Zaefferer, S. Computer-aided crystallographic analysis in the TEM. *Adv. Imaging Electron Phys.* **125**, 356–415 (2002).
53. Cullity, B. D. *Elements of X-ray Diffraction* (Addison-Wesley Publishing, 1956).
54. Plimpton, S. Fast Parallel Algorithms for Short-Range Molecular Dynamics. *J. Comput. Phys.* **117**, 1–19 (1995).
55. Ackland, G. J. Theoretical study of titanium surfaces and defects with a new many-body potential. *Philos. Mag. A* **66**, 917–932 (1992).
56. Stukowski, A. Visualization and analysis of atomistic simulation data with OVITO—the Open Visualization Tool. *Modell. Simul. Mater. Sci. Eng.* **18**, 015012 (2010).
57. Song, J., Fan, C., Ma, H., Liang, L. & Wei, Y. Crack deflection occurs by constrained microcracking in nacre. *Acta Mech. Sin.* **34**, 143–150 (2017).
58. Salas, C., Bueno-Perez, J. D., Lopez-Tellez, J. F. & Checa, A. G. Form and function of the mantle edge in Protobranchia (Mollusca: Bivalvia). *Zoology* **153**, 126027 (2022).
59. Mine, Y., Ando, S. & Takashima, K. Crystallographic fatigue crack growth in titanium single crystals. *Mater. Sci. Eng., A* **528**, 7570–7578 (2011).
60. Robinson, J. & Beevers, C. The effects of load ratio, interstitial content, and grain size on low-stress fatigue-crack propagation in α -titanium. *Met. Sci. J.* **7**, 153–159 (1973).
61. Hasib, M. T., Ostergaard, H. E., Liu, Q., Li, X. & Kruzic, J. J. Tensile and fatigue crack growth behavior of commercially pure titanium

- produced by laser powder bed fusion additive manufacturing. *Addit. Manuf.* **45**, 102027 (2021).
62. Wanhill, R. Environmental fatigue crack propagation in medium strength titanium sheet alloys. *Eng. Fract. Mech.* **6**, 681–697 (1974).
63. Hübner, P., Kiessling, R., Biermann, H. & Vinogradov, A. Fracture behaviour of ultrafine-grained materials under static and cyclic loading. *Int. J. Mater. Res.* **97**, 1566–1570 (2006).
64. Wang, Q., Sun, Q., Xiao, L. & Sun, J. Effect of surface nanocrystallization on fatigue behavior of pure titanium. *J. Mater. Eng. Perform.* **25**, 241–249 (2016).
65. Loh, H.-C. et al. Nacre toughening due to cooperative plastic deformation of stacks of co-oriented aragonite platelets. *Commun. Mater.* **1**, 77 (2020).

Acknowledgements

We thank C. Xu and D. Pan for assistance in performing in-situ fatigue crack growth experiments. This work was supported by the National Key Research and Development Project (No. 2022YFB4600019, 2023YFB3712100), National Natural Science Foundation of China (No. U21B2077, No. 52275147, No. 52321002, No. 52222505, No. 52122505), Natural Science Foundation of Shanghai (No. 23ZR1415500)

Author contributions

Conceptualization: Yong.Z., Q.Y., X.-C.Z., B.S., R.O.R. and S.-T.T. Methodology: Yong.Z. and X.L. Investigation: Yong.Z., C.H., X.L., X.W., Yin.Z, J.W, Y.J. and B.S. Visualization: Yong.Z., C.H., Q.Y. and B.S. Resources: X.W., C.J., Y.J., X.-C.Z. and S.-T.T. Funding acquisition: X.-C.Z. and S.-T.T. Project administration: X.-C.Z. and S.-T.T. Supervision: Q.Y., X.-C.Z., B.S., R.O.R. and S.-T.T. Writing – original draft: Yong.Z. and B.S. Writing – review & editing: C.H., Q.Y., X.-C.Z., and R.O.R.

Competing interests

The authors declare no competing interests.

Additional information

Supplementary information The online version contains supplementary material available at <https://doi.org/10.1038/s41467-024-51423-5>.

Correspondence and requests for materials should be addressed to Xian-Cheng Zhang, Binhan Sun or Robert O. Ritchie.

Peer review information *Nature Communications* thanks Jean-Bernard Vogt and the other, anonymous, reviewer(s) for their contribution to the peer review of this work. A peer review file is available.

Reprints and permissions information is available at <http://www.nature.com/reprints>

Publisher's note Springer Nature remains neutral with regard to jurisdictional claims in published maps and institutional affiliations.

Open Access This article is licensed under a Creative Commons Attribution-NonCommercial-NoDerivatives 4.0 International License, which permits any non-commercial use, sharing, distribution and reproduction in any medium or format, as long as you give appropriate credit to the original author(s) and the source, provide a link to the Creative Commons licence, and indicate if you modified the licensed material. You do not have permission under this licence to share adapted material derived from this article or parts of it. The images or other third party material in this article are included in the article's Creative Commons licence, unless indicated otherwise in a credit line to the material. If material is not included in the article's Creative Commons licence and your intended use is not permitted by statutory regulation or exceeds the permitted use, you will need to obtain permission directly from the copyright holder. To view a copy of this licence, visit <http://creativecommons.org/licenses/by-nc-nd/4.0/>.

© The Author(s) 2024